

# Broadband optical conductivity of the chiral multifold semimetal PdGa

L. Z. Maulana,<sup>1</sup> Z. Li,<sup>2</sup> E. Uykur,<sup>1</sup> K. Manna,<sup>3,4</sup> S. Polatkan,<sup>1</sup> C. Felser,<sup>3</sup> M. Dressel,<sup>1</sup> and A. V. Pronin<sup>1,\*</sup>

<sup>1</sup>*Physikalisches Institut, Universität Stuttgart, 70569 Stuttgart, Germany*

<sup>2</sup>*MIIT Key Laboratory of Advanced Display Materials and Devices,  
Ministry of Industry and Information Technology, Institute of Optoelectronics and Nanomaterials,  
Nanjing University of Science and Technology, Nanjing 210094, China*

<sup>3</sup>*Max-Planck-Institut für Chemische Physik fester Stoffe, 01187 Dresden, Germany*

<sup>4</sup>*Department of Physics, Indian Institute of Technology Delhi, Hauz Khas, New Delhi 110016, India*

(Dated: March 29, 2021)

We present an optical conductivity study of the multifold semimetal PdGa, performed in a broad spectral range ( $100 - 20000 \text{ cm}^{-1}$ ;  $12 \text{ meV} - 2.5 \text{ eV}$ ) down to  $T = 10 \text{ K}$ . The conductivity at frequencies below  $4000 \text{ cm}^{-1}$  is dominated by free carriers while at higher frequencies interband transitions provide the major contribution. The spectra do not demonstrate a significant temperature evolution: only the intraband part changes as a function of temperature with the plasma frequency remaining constant. The interband contribution to the conductivity exhibits a broad peak at around  $5500 \text{ cm}^{-1}$  and increases basically monotonously at frequencies above  $9000 \text{ cm}^{-1}$ . The band-structure-based computations reproduce these features of the interband conductivity and predict its linear-in-frequency behavior as frequency diminishes.

## I. INTRODUCTION

The solid-state realization of massless Weyl fermions was first theoretically discussed [1, 2] and subsequently experimentally confirmed in TaAs [3, 4], one of the materials belonging to a broad, by now, class of solids known as topological Weyl semimetals. Since these discoveries, various families of other topological semimetals – materials with the nontrivial band topology relevant for the bulk states – were unveiled [5–9]. One particular example is multifold semimetals. In these compounds, the topologically protected band crossings of degeneracy higher than two are described by Weyl-like Hamiltonians: linear in momentum and in effective spin, which can be larger than  $1/2$  [10, 11].

Recently, a number of compounds from the cubic space group 198 (SG198), which is non-centrosymmetric and has no mirror planes, were confirmed to possess such multifold crossing points [12–20]. In these materials, the band crossings with different chiralities are situated at different energy positions, providing thus a realization of electronic chiral crystals. Remarkably, the crystals of these compounds can be grown as single enantiomers, i.e., with a given crystalline and electronic chirality [20, 21].

Generally, optics seems to be an ideal tool for studying chiral materials and for manipulating the chiral degrees of freedom, as the circularly polarized light can be directly coupled to the chiral quasiparticles within such solids. For such investigations, it is essential to possess an advance knowledge of the linear optical response for the materials of interest. In other families of topological semimetals, optical spectroscopy, a genuine bulk-

sensitive technique, was shown to provide insight into the bulk electronic properties [9, 22]. Thus, efforts were recently taken to calculate and to measure the frequency-dependent conductivity,  $\sigma(\omega) = \sigma_1(\omega) + i\sigma_2(\omega)$ , of the chiral multifold compounds. Specifically, the optical conductivity of two members of this family, RhSi and CoSi, was studied theoretically [23, 24] and experimentally [25–29]. Linear-in-frequency conductivity  $\sigma_1(\omega)$  due to interband transitions at low frequencies was evidenced in both RhSi and CoSi, consistent with theory predictions for multifold semimetals [30] and with general expectations for interband optical conductivity in linearly dispersing three-dimensional electronic bands [31–33]. In this paper, we expand the experimental studies of  $\sigma(\omega)$  to another multifold semimetal, PdGa. Recently, this compound was thoroughly studied by ARPES [20] and scanning tunneling microscopy [21], and a very high Chern number,  $|C| = 4$ , was evidenced in these studies.

## II. EXPERIMENT

PdGa single crystals were grown from its melt by a self-flux technique, as described in Refs. [20, 21]. First, a polycrystalline ingot was prepared using the arc melt technique with a stoichiometric mixture of high-purity Pd and Ga. Then, the crushed powder was filled in a thin-wall alumina crucible and finally sealed in a quartz ampoule. The crystal growth was done under a partial vacuum of 3 mbar. The ampoules were heated to  $1100 \text{ }^\circ\text{C}$ , kept there for 12 h, and then slowly cooled to  $900 \text{ }^\circ\text{C}$  at a rate of  $1.5 \text{ }^\circ\text{C/h}$ . Finally, the samples were cooled to  $800 \text{ }^\circ\text{C}$  at a rate of  $50 \text{ }^\circ\text{C/h}$ , annealed for 120 h and then cooled to  $500 \text{ }^\circ\text{C}$  at a rate of  $5 \text{ }^\circ\text{C/h}$ . PdGa single crystals with average linear dimensions of a few

\* artem.pronin@pi1.physik.uni-stuttgart.de

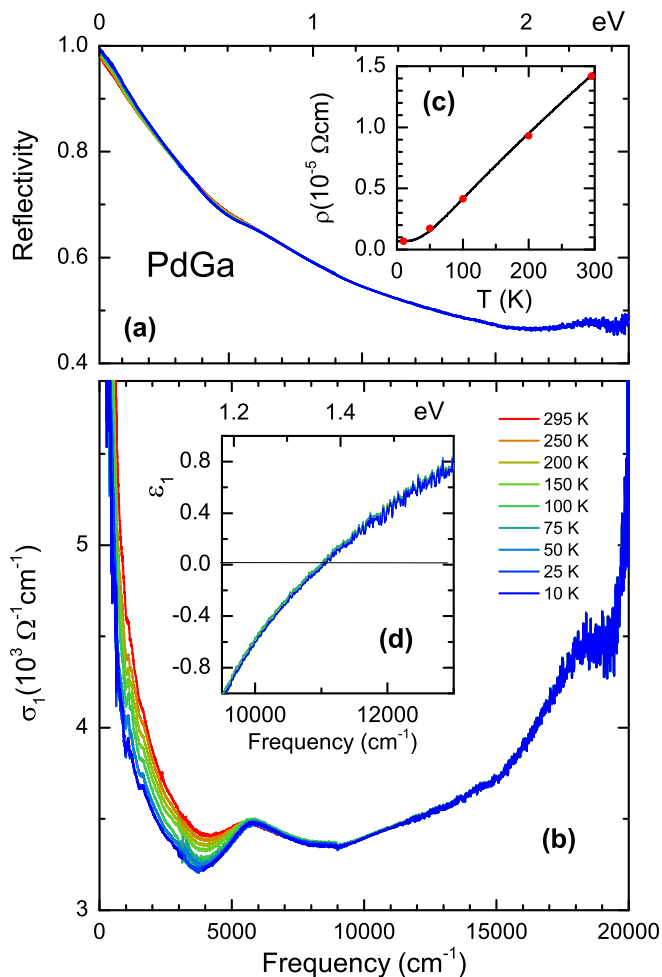


FIG. 1. PdGa optical reflectivity (a) and the real part of optical conductivity (b) at selected temperatures as indicated. The insets show (c) the dc resistivity vs  $T$  (line) together with the inverse optical conductivity in the  $\nu \rightarrow 0$  limit used in the fits of Fig. 2 (bold dots) and (d) zoomed permittivity spectra near the zero-line crossing. Note that in (a), (b), and (d), the experimental curves are presented for all indicated temperatures.

mm were obtained.

The crystals were first analyzed with a white beam backscattering Laue x-ray diffractometer at room temperature. The obtained single and sharp Laue spot could be indexed by a single pattern, revealing the excellent quality of the grown single-enantiomer crystals without any twinning or domains, see the Supplemental Material below for a Laue-pattern example. The structural parameters were determined using a Rigaku AFC7 four-circle diffractometer with a Saturn 724+ CCD-detector applying graphite-monochromatized Mo- $K\alpha$  radiation. The crystal structure was refined to be cubic  $P2_13$  (SG198) with a lattice constant  $a=4.896$  Å.

Temperature-dependent transport measurements (longitudinal dc resistivity and Hall) were performed in custom-made setups at temperatures down to 2 K.

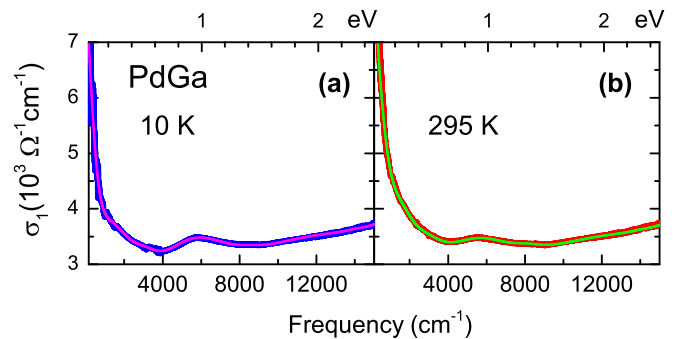


FIG. 2. Drude-Lorentz fits (lines) of the measured optical conductivity spectra (symbols) at 10 and 295 K.

Temperature-dependent ( $T = 10 - 295$  K) optical reflectivity,  $R(\nu)$ , was measured on a PdGa single crystal (with roughly  $1.5 \times 1.5$  mm<sup>2</sup> in lateral dimensions) over a broad frequency range from  $\nu = \omega/(2\pi) = 100$  to 20000 cm<sup>-1</sup> (12 meV – 3 eV). The spectra in the far-infrared (below 700 cm<sup>-1</sup>) were collected with a Bruker IFS 113v Fourier-transform spectrometer using an *in situ* freshly evaporated gold over-filming technique for reference measurements. At higher frequencies, a Bruker Hyperion infrared microscope attached to a Bruker Vertex 80v FTIR spectrometer was used. For these measurements, freshly evaporated gold mirrors on glass substrates served as the reference. No sample anisotropy was detected, which is in agreement with the cubic crystallographic structure.

For the Kramers-Kronig analysis, the zero-frequency extrapolations were made using the Hagen-Rubens relation in accordance with temperature-dependent longitudinal dc resistivity measurements. For high-frequency extrapolations, we utilized x-ray atomic scattering functions [34] followed by the free-electron behavior,  $R(\omega) \propto 1/\omega^4$ , above 30 keV.

### III. CALCULATIONS

The band structure and optical properties of PdGa were calculated by first-principles calculations based on the density-functional theory with the Perdew-Burke-Ernzerhof exchange-correlation functional implemented in Quantum ESPRESSO [35]. Norm-conserving pseudopotentials with the generalized gradient approximation (GGA) are adopted in this work. We used the experimental structural parameters [21] without any geometry optimization. The energy cutoff of  $35.0R_y$  and a  $k$ -point grid with  $24 \times 24 \times 24$  ( $40 \times 40 \times 40$ ) points were adopted for the band-structure (optical-properties) calculations. The spin-orbit-coupling effect as well as a frequency-independent broadening for interband transitions due to electron scattering (0.2 eV) were included in the calculations.

#### IV. RESULTS AND DISCUSSION

Examples of the frequency-dependent optical spectra are shown in Fig. 1 for selected temperatures. The raw reflectivity shows typical metallic behavior with  $R(\nu)$  approaching unity as frequency diminishes, see panel (a). The spectra of the real part of optical conductivity [panel (b)] demonstrate corresponding behavior:  $\sigma_1$  increases as  $\nu \rightarrow 0$ . This is in qualitative agreement with a simple free-electron Drude model. The screened plasma frequency of free electrons,  $\nu_{pl}^{scr}$ , can be estimated from the zero crossings of the permittivity spectra,  $\epsilon_1(\nu) = 1 - 2\sigma_2(\nu)/\nu$ , shown in panel (d). We found  $\nu_{pl}^{scr}$  to be temperature independent at  $\nu_{pl}^{scr} \simeq 11\,000\text{ cm}^{-1}$ , corresponding to  $\hbar\omega_{pl}^{scr} = 1.37\text{ eV}$ .

Comparing these findings with the experimental results on  $\nu_{pl}^{scr}$  in many other nodal semimetals [25, 27, 28, 36–41], one can immediately notice a very large value of  $\nu_{pl}^{scr}$  in PdGa. For example, it is roughly one order of magnitude larger, than in the sister compounds, the multifold semimetals RhSi,  $\nu_{pl}^{scr} \sim 1500 - 1700\text{ cm}^{-1}$  [27, 29], and CoSi,  $\nu_{pl}^{scr} \sim 600 - 800\text{ cm}^{-1}$  [25, 28]. This “metallicity” of PdGa is obviously related to its band structure with the chemical potential situated far from the nodes, as discussed below. Our Hall measurements (see the Supplemental Material) also reveal the metallic nature of PdGa: its electron density is high and almost temperature-independent,  $n = (3 \pm 1) \times 10^{22}\text{ cm}^{-3}$ .

As seen in Fig. 1, the overall temperature evolution of the conductivity spectra is rather weak: only the low-energy free-electron part shows detectable  $T$ -induced changes due to the temperature-dependent electron scattering, in agreement with the metal-like optical response. At  $\nu > 4000\text{ cm}^{-1}$ , the interband transitions start to become visible in  $\sigma_1(\nu)$ .

To analyze the optical spectra in a more quantitative

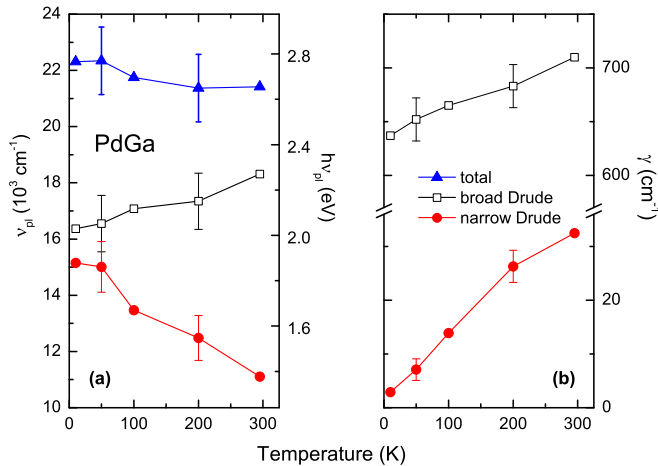


FIG. 3. Temperature-dependent parameters of the two Drude terms (narrow and broad) used in the Drude-Lorentz fits. Note different vertical scales for the plasma frequencies (a) and the scattering rates (b).

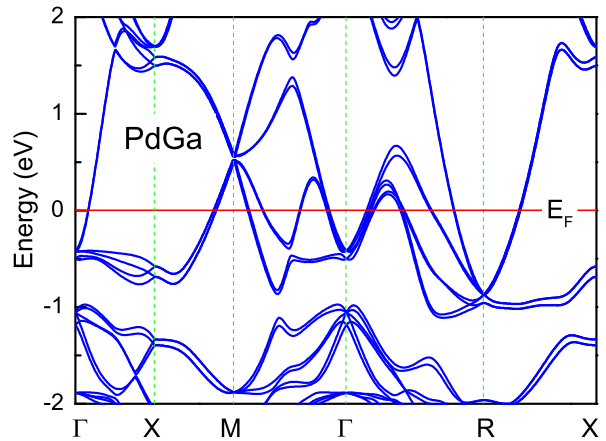


FIG. 4. Low-energy electronic band structure of PdGa with the spin-orbit coupling included. The multifold fermions are supposed to exist near the  $\Gamma$  and  $R$  points.

way, we first performed a standard Drude-Lorentz fit [42] for a number of temperatures. The Drude contribution describes the intraband response, while the Lorentzians are used to fit the interband optical transitions. Examples of such fits are presented in Fig. 2. In all the fits, we kept the zero-frequency limit of optical conductivity equal to the measured dc-conductivity value at every temperature, see Fig. 1(c). No other restrictions on the fit parameters were imposed. The fits were obtained by the simultaneous fitting of  $R(\nu)$ ,  $\sigma_1(\nu)$  and  $\epsilon_1(\nu)$ .

We found that we need at least two Drude components (“narrow” and “broad”) with different scattering rates to provide accurate Drude-Lorentz fits to the experimental spectra. This approach is often used to describe the intraband optical response in different multiband materials [27, 29, 43–49], but the exact interpretation of the two Drude terms remains arguable [27, 29, 46]. PdGa possesses not two, but many different bands crossing the Fermi level, see Figs. 4 and 5. Hence, the two components might be associated, e.g., with two different sets of bands, or with different scattering mechanisms. In any case, the two-Drude approach utilized here should be considered just as a minimalist model to fit the intraband optical response in a Kramers-Kronig consistent way and to extract the total spectral weight (the plasma frequency) of itinerant carriers.

The fit parameters of the Drude terms are shown in Fig. 3 as functions of temperature. Because of the temperature-induced redistribution of the spectral weight between the terms, neither of the scattering rates ( $\gamma$ ) is expected to follow the dc-resistivity temperature dependence accurately. Nevertheless, it is primarily the temperature variation of the narrow-Drude scattering rate, which provides the reconciliation of the relatively strong temperature dependence of dc conductivity [the residual resistivity ratio is around 20, see Fig. 1(c)] and the fairly weak temperature evolution of intraband optical conductivity; see also the Supplemental Material.

While the parameters of the Drude terms vary appreciably with temperature, the total intraband unscreened plasma frequency  $\nu_{pl}$  remains almost temperature independent at  $\sim 21\,800\text{ cm}^{-1}$  ( $\hbar\omega_{pl} \approx 2.7\text{ eV}$ ). This value is significantly larger than the one reported for RhSi ( $\sim 11\,300\text{ cm}^{-1}$  or  $1.4\text{ eV}$ ) [27], that is in qualitative agreement with the smaller bulk Fermi surface of RhSi, see the Supplemental Material. Also, the fit-based  $\nu_{pl}$  in PdGa is consistent with the screened plasma frequency  $\nu_{pl}^{scr}$ , obtained from zero crossings of  $\varepsilon_1(\nu)$ , if the higher-frequency dielectric constant  $\varepsilon_\infty$  is assumed to be around 1.4, which is a reasonable value [cf. Fig. 1 (d)]. We recall that  $\nu_{pl}^{scr} = \nu_{pl}/\sqrt{\varepsilon_\infty}$ .

For a more elaborative analysis, we performed band-structure calculations for PdGa and then computed its interband optical conductivity, as described above. The results of the band-structure calculations are shown in Fig. 4. It is apparent that the Fermi level  $E_F$  crosses a number of electron- and hole-like bands and that the multifold nodes near the  $\Gamma$  and  $R$  points are situated quite deep ( $0.5\text{ eV}$  or more) below  $E_F$ . Hence, PdGa possesses an extended bulk Fermi surface, which occupies a significant portion of the Brillouin zone, see Fig. 5.

The large bulk Fermi surface and the consequent intense intraband optical response make a direct comparison between the interband conductivity computed from the band structure and the experimental spectra challenging. As seen from Fig. 6, the interband portion of optical conductivity is not zero down to very low frequency. This might look surprising, as usually there is an onset (a Pauli edge) in the interband-conductivity spectra for systems with the Fermi level situated far from the nodes, which is the case for PdGa. However, PdGa possess multiple bands with small energy separation, which (the bands) cross the Fermi level, see Fig. 4 and the inset of Fig. 6. The cumulative effect of the transitions between these bands causes the quasilinearity of the interband  $\sigma_1(\nu)$  in PdGa at low frequencies. We note that at  $\nu \rightarrow 0$ ,  $\sigma_1(\nu)$  flattens out. More details on band-selective optical transitions in PdGa can be found in Ref. [50].

In order to compare the experimental and computed interband conductivity, the intraband (Drude) response

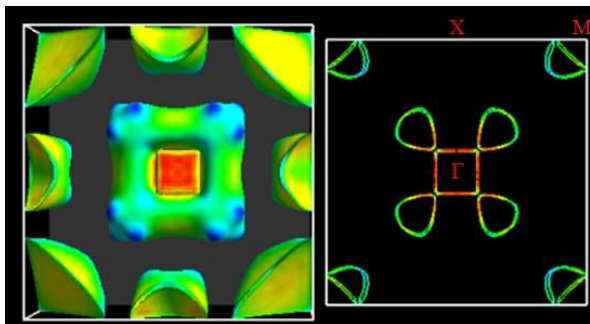


FIG. 5. Calculated bulk Fermi surface of PdGa (left) and its cut at the middle of the Brillouin zone (right). The  $k_z$  direction is perpendicular to the picture plane.

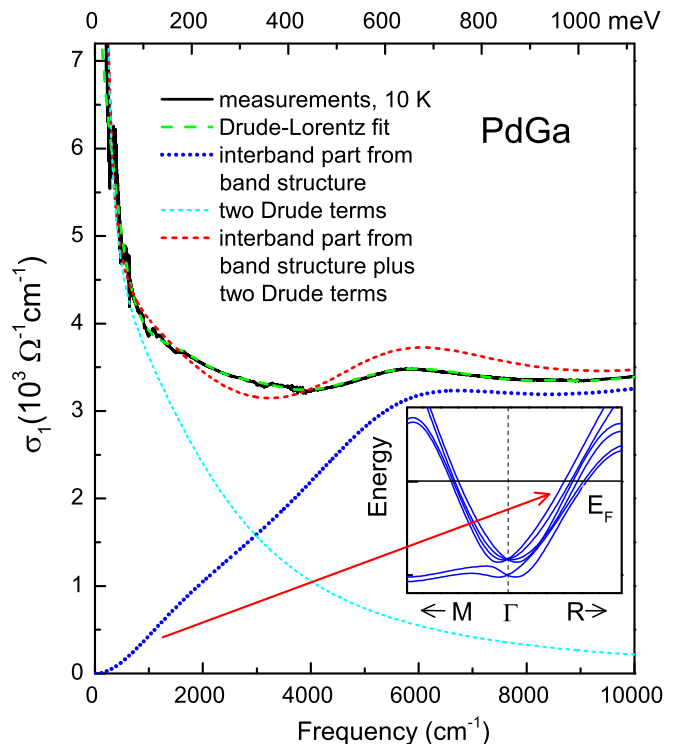


FIG. 6. Comparison of the measured (solid line) and calculated (dashed and dotted lines) optical conductivity in PdGa. The interband portion of  $\sigma_1(\omega)$  (blue dotted line) is calculated from the band structure. Adding two Drude terms (cyan dashed line) to this curve provides a good qualitative match (red dashed line) to the experimental spectrum. The green dashed line is the fit from Fig. 2. The quasilinear interband conductivity at low frequencies is due to the transitions between the multiple bands in the vicinity of the Fermi level, as shown in the inset.

can be subtracted from the former spectra, as it was done, e.g., in Refs. [27, 29, 51, 52]. This procedure may obviously produce ambiguities in determining the interband portion of the experimental  $\sigma_1(\nu)$ , especially at the lowest frequencies, where the interband conductivity is low. Hence, we followed a slightly different approach: instead of subtracting the Drude terms from the experimental spectra, we added them to the calculated interband conductivity. Basically, we performed a sort of fit with two Drude terms and the interband  $\sigma_1(\nu)$  obtained from the band structure with a frequency-independent electron scattering rate of  $0.2\text{ eV}$  ( $\sim 1600\text{ cm}^{-1}$ ). The results of this analysis are shown in Fig. 6 as well as in the Supplemental Material. As a starting point, we used the Drude terms, obtained from our Drude-Lorentz fits (Fig. 2). For the best possible description of the experimental spectra, we had to slightly change the parameters of these terms, but the zero-frequency limit of  $\sigma_1(\nu)$  remained to be equal to the inverse of the measured dc resistivity.

Having in mind that the band-structure-based computations of  $\sigma_1(\nu)$  generally reproduce the experimental

findings only qualitatively [22, 27, 38, 40, 41, 51], the match between theory and experiment can be considered as rather good: in the present case the general conductivity level observed in experiment is reproduced by computations and the major feature of the interband  $\sigma_1(\nu)$  – the flat maximum at around  $5500\text{ cm}^{-1}$  – is seen in both computed and measured spectra. The remaining discrepancies can be attributed, e.g., to a frequency-dependent electron scattering in the investigated sample (as noticed above, we assumed a frequency-independent scattering rate in our computations).

Due to the very high free-carrier concentration and relatively large electron scattering (the broad Drude component), direct experimental verification of the linear interband optical conductivity at low energies, as it is predicted by theory for multifold semimetals with the nodes situated in the vicinity of  $E_F$  [30], is impossible for PdGa. Nevertheless, our experimental spectra can be well described as a sum of the interband conductivity, obtained from the band structure, and a strong Drude-like free-carrier contribution. Let us also note that this strong electronic response prevents observation of any phonon modes on the top of it (based on its crystallographic symmetry, PdGa is supposed to have five infrared-active phonons).

## V. CONCLUSIONS

We have studied the broadband optical conductivity of the multifold semimetal PdGa. A prominent metallic response is detected. The free-carrier Drude-like contribution with a temperature-independent plasma frequency ( $\hbar\omega_{pl}^{scr} = 1.37\text{ eV}$ ) dominates the spectra at frequencies below  $4000\text{ cm}^{-1}$ , preventing direct detection of the linear-in-frequency interband conductivity predicted for the multifold semimetals. At higher frequencies, the spectra calculated from the band structure reproduce the experimental spectra. Namely, the general conductivity levels obtained in experiments and in computations match each other and the frequency position of the most prominent feature in the experimental interband conductivity – the maximum at around  $5500\text{ cm}^{-1}$  ( $680\text{ meV}$ ) – is reproduced by the computations.

## VI. ACKNOWLEDGMENTS

We thank Gabriele Untereiner for valuable technical support. E.U. acknowledges financial support from the European Social Fund and from the Ministry of Science, Research, and the Arts of Baden-Württemberg. K.M. and C.F. acknowledge financial support from the European Research Council (ERC) via Advanced Grant No. 742068 “TOP-MAT”. The work in Stuttgart was partly supported by the Deutsche Forschungsgemeinschaft (DFG) via Grant No. DR228/51-3.

## VII. SUPPLEMENTAL MATERIAL

**Material and sample characterization.** The results of our Laue and Hall measurements are presented in Figs. 7 and 8.

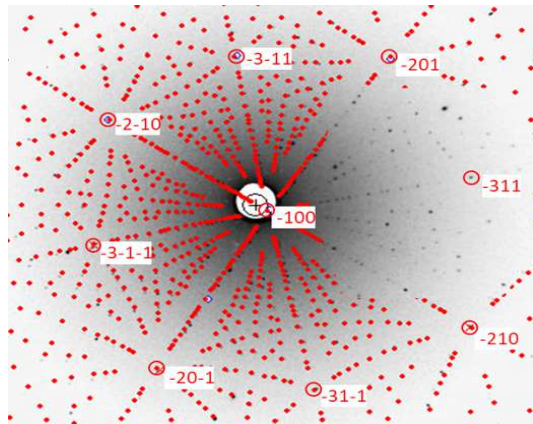


FIG. 7. Laue pattern of a PdGa single crystal, superposed with a simulated pattern.

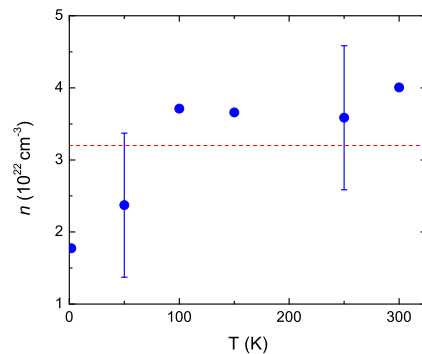


FIG. 8. Carrier concentration in the PdGa sample used in the optical experiments versus temperature, as obtained from Hall measurements. The dashed horizontal line shows the averaged value.

**Two-component Drude fits.** In order to demonstrate how the low-frequency portion of the measured optical conductivity and the dc-conductivity value are reconciled in our fits, we re-plot the 10-K experimental spectrum and its fit shown in Fig. 6 on a double-logarithmic scale in Fig. 9.

**Comparison of the Fermi surfaces of PdGa and RhSi.** The bulk Fermi surfaces of PdGa and RhSi were calculated using WIEN2k’s [53] full-potential linearized augmented plane wave methods with the Perdew-Burke-Ernzerhof exchange-correlation functional on a  $32 \times 32 \times 32$   $k$ -mesh, with account for spin-orbit coupling and with the lattice parameters taken from Ref. [21]. The results of these calculations are shown in Fig. 10.

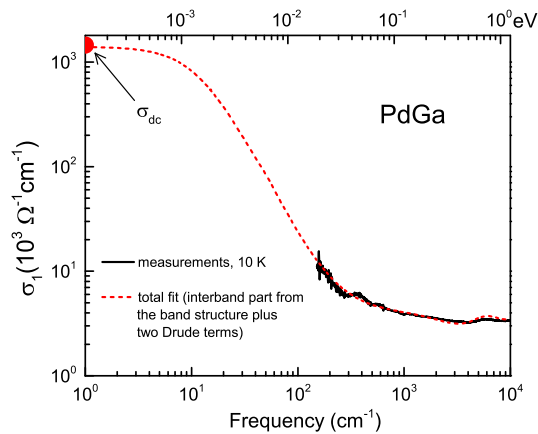


FIG. 9. Same graphs as shown in Fig. 6 (the 10-K conductivity data and its fit) on a double-logarithmic scale. The dc conductivity value is shown as a bold red dot on the left vertical axis.

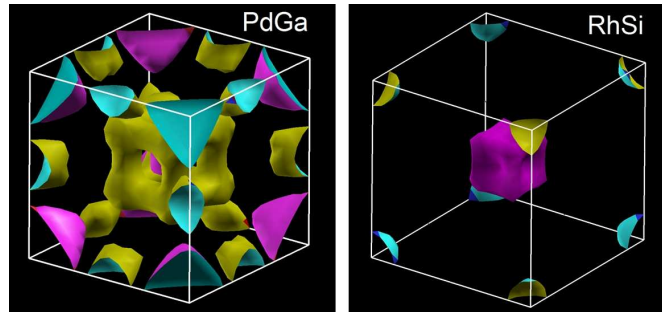


FIG. 10. Bulk Fermi surfaces of PdGa (left) and RhSi (right).

- 
- [1] S. Murakami, Phase transition between the quantum spin Hall and insulator phases in 3D: emergence of a topological gapless phase, *New J. Phys.* **9**, 356 (2007).
- [2] X. Wan, A. M. Turner, A. Vishwanath, and S. Y. Savrasov, Topological semimetal and Fermi-arc surface states in the electronic structure of pyrochlore iridates, *Phys. Rev. B* **83**, 205101 (2011).
- [3] B. Q. Lv, H. M. Weng, B. B. Fu, X. P. Wang, H. Miao, J. Ma, P. Richard, X. C. Huang, L. X. Zhao, G. F. Chen, Z. Fang, X. Dai, T. Qian, and H. Ding, Experimental Discovery of Weyl Semimetal TaAs, *Phys. Rev. X* **5**, 031013 (2015).
- [4] S.-Y. Xu, I. Belopolski, N. Alidoust, M. Neupane, G. Bian, C. Zhang, R. Sankar, G. Chang, Z. Yuan, C.-C. Lee, S.-M. Huang, H. Zheng, J. Ma, D. S. Sanchez, B. K. Wang, A. Bansil, F. Chou, P. P. Shibayev, H. Lin, S. Jia, and M. Z. Hasan, Discovery of a Weyl fermion semimetal and topological Fermi arcs, *Science* **349**, 613 (2015).
- [5] A. A. Burkov, M. D. Hook, and L. Balents, Topological nodal semimetals, *Phys. Rev. B* **84**, 235126 (2011).
- [6] Z. Zhu, G. W. Winkler, Q. S. Wu, J. Li, and A. A. Soluyanov, Triple Point Topological Metals, *Phys. Rev. X* **6**, 031003 (2016).
- [7] T. Bzdušek, Q. S. Wu, A. Rüegg, M. Sigrist, and A. A. Soluyanov, Nodal-chain metals, *Nature* **538**, 75 (2016).
- [8] A. A. Burkov, Topological semimetals, *Nat. Mater.* **15**, 1145 (2016).
- [9] N. P. Armitage, E. J. Mele, and A. Vishwanath, Weyl and Dirac semimetals in three-dimensional solids, *Rev. Mod. Phys.* **90**, 015001 (2018).
- [10] J. L. Mañes, Existence of bulk chiral fermions and crystal symmetry, *Phys. Rev. B* **85**, 155118 (2012).
- [11] B. Bradlyn, J. Cano, Z. Wang, M. G. Vergniory, C. Felser, R. J. Cava, B. A. Bernevig, Beyond Dirac and Weyl fermions: Unconventional quasiparticles in conventional crystals, *Science* **353**, aaf5037 (2016).
- [12] G. Chang, B. J. Wieder, F. Schindler, D. S. Sanchez, I. Belopolski, S.-M. Huang, B. Singh, D. Wu, T.-R. Chang, T. Neupert, S.-Y. Xu, H. Lin, and M. Z. Hasan, Topological quantum properties of chiral crystals, *Nat. Mater.* **17**, 978 (2018).
- [13] G. Chang, S.-Y. Xu, B. J. Wieder, D. S. Sanchez, S.-M. Huang, I. Belopolski, T.-R. Chang, S. Zhang, A. Bansil, H. Lin, and M. Z. Hasan, Unconventional chiral fermions and large topological Fermi arcs in RhSi, *Phys. Rev. Lett.* **119**, 206401 (2017).
- [14] P. Tang, Q. Zhou, and S.-C. Zhang, Multiple types of topological fermions in transition metal silicides, *Phys. Rev. Lett.* **119**, 206402 (2017).
- [15] D. S. Sanchez, I. Belopolski, T. A. Cochran, X. Xu, J.-X. Yin, G. Chang, W. Xie, K. Manna, V. Süß, C.-Y. Huang, N. Alidoust, D. Multer, S. S. Zhang, N. Shumiya, X. Wang, G.-Q. Wang, T.-R. Chang, C. Felser, S.-Y. Xu, S. Jia, H. Lin, and M. Z. Hasan, Topological chiral crystals with helicoid-arc quantum states, *Nature* **567**, 500 (2019).
- [16] Z. Rao, H. Li, T. Zhang, S. Tian, C. Li, B. Fu, C. Tang, L. Wang, Z. Li, W. Fan, J. Li, Y. Huang, Z. Liu, Y. Long, C. Fang, H. Weng, Y. Shi, H. Lei, Y. Sun, T. Qian, and H. Ding, Observation of unconventional chiral fermions with long Fermi arcs in CoSi, *Nature* **567**, 496 (2019).
- [17] D. Takane, Z. Wang, S. Souma, K. Nakayama, T. Nakamura, H. Oinuma, Y. Nakata, H. Iwasawa, C. Cacho, T. Kim, K. Horiba, H. Kumigashira, T. Takahashi, Y. Ando, and T. Sato, Observation of chiral fermions with a large topological charge and associated Fermi-arc surface states in CoSi, *Phys. Rev. Lett.* **122**, 076402 (2019).
- [18] N. B. M. Schröter, D. Pei, M. G. Vergniory, Y. Sun, K. Manna, F. de Juan, J. A. Krieger, V. Süß, M. Schmidt, P. Dudin, B. Bradlyn, T. K. Kim, T. Schmitt, C. Cacho, C. Felser, V. N. Strocov, and Y. Chen, Chiral topological semimetal with multifold band crossings and long Fermi arcs, *Nat. Phys.* **15**, 759 (2019).
- [19] M. Yao, K. Manna, Q. Yang, A. Fedorov, V. Voroshnin, B. V. Schwarze, J. Hornung, S. Chattopadhyay, Z. Sun, S. N. Guin, J. Wosnitza, H. Borrmann, C. Shekhar, N. Kumar, J. Fink, Y. Sun, and Claudia Felser, Observation of giant spin-split Fermi-arc with maximal Chern number

- in the chiral topological semimetal PtGa, *Nat. Commun.* **11**, 2033 (2020).
- [20] N. B. M. Schröter, S. Stolz, K. Manna, F. de Juan, M. G. Vergniory, J. A. Krieger, D. Pei, T. Schmitt, P. Dudin, T. K. Kim, C. Cacho, B. Bradlyn, H. Borrmann, M. Schmidt, R. Widmer, V. N. Stokov, C. Felser, Observation and control of maximal Chern numbers in a chiral topological semimetal, *Science* **369**, 179 (2020).
- [21] P. Sessi, F.-R. Fan, F. Küster, K. Manna, N. B. M. Schröter, J.-R. Ji, S. Stolz, J. A. Krieger, D. Pei, T. K. Kim, P. Dudin, C. Cacho, R. Widmer, H. Borrmann, Wu. Shi, K. Chang, Y. Sun, C. Felser, and S. S. P. Parkin, Handedness-dependent quasiparticle interference in the two enantiomers of the topological chiral semimetal PdGa, *Nat. Commun.* **11**, 3507 (2020).
- [22] A. V. Pronin and M. Dressel, Nodal Semimetals: A Survey on Optical Conductivity, *Phys. Status Solidi B* **258**, 2000027 (2021).
- [23] Z. Li, T. Iitaka, H. Zeng, and H. Su, Optical response of the chiral topological semimetal RhSi, *Phys. Rev. B* **100**, 155201 (2019).
- [24] T. Habe, Dynamical conductivity in the multiply degenerate point-nodal semimetal CoSi, *Phys. Rev. B* **100**, 245131 (2019).
- [25] D. van der Marel, A. Damascelli, K. Schulte, A. A. Menovsky, Spin, charge, and bonding in transition metal mono-silicides, *Physica B* **244**, 138 (1998).
- [26] D. Rees, K. Manna, B. Lu, T. Morimoto, H. Borrmann, C. Felser, J. E. Moore, D. H. Torchinsky, and J. Orenstein, Helicity-dependent photocurrents in the chiral Weyl semimetal RhSi, *Sci. Adv.* **6**, eaba0509 (2020).
- [27] L. Z. Maulana, K. Manna, E. Uykur, C. Felser, M. Dressel, and A. V. Pronin, Optical conductivity of multifold fermions: The case of RhSi, *Phys. Rev. Research* **2**, 023018 (2020).
- [28] B. Xu, Z. Fang, M. A. Sánchez-Martínez, J. W. F. Venderbos, Z. Ni, T. Qiu, K. Manna, K. Wang, J. Paglione, C. Bernhard, C. Felser, E. J. Mele, A. G. Grushin, A. M. Rappe, and L. Wu, Optical signatures of multifold fermions in the chiral topological semimetal CoSi, *PNAS* **117**, 27104 (2020).
- [29] Z. Ni, B. Xu, M. A. Sánchez-Martínez, Y. Zhang, K. Manna, C. Bernhard, J. W. F. Venderbos, F. de Juan, C. Felser, A. G. Grushin, and L. Wu, Linear and nonlinear optical responses in the chiral multifold semimetal RhSi, *npj Quantum Materials* **5**, 96 (2020).
- [30] M.-Á. Sánchez-Martínez, F. de Juan, and A. G. Grushin, Linear optical conductivity of chiral multifold fermions, *Phys. Rev. B* **99**, 155145 (2019).
- [31] P. Hosur, S. A. Parameswaran, and A. Vishwanath, Charge transport in Weyl semimetals, *Phys. Rev. Lett.* **108**, 046602 (2012).
- [32] Á. Bácsı and A. Virosztek, Low-frequency optical conductivity in graphene and in other scale-invariant two-band systems, *Phys. Rev. B* **87**, 125425 (2013).
- [33] P. E. C. Ashby and J. P. Carbotte, Chiral anomaly and optical absorption in Weyl semimetals, *Phys. Rev. B* **89**, 245121 (2014).
- [34] D. B. Tanner, Use of x-ray scattering functions in Kramers-Kronig analysis of reflectance, *Phys. Rev. B* **91**, 035123 (2015).
- [35] P. Giannozzi, S. Baroni, N. Bonini, M. Calandra, R. Car, C. Cavazzoni, D. Ceresoli, G. L. Chiarotti, M. Cocconi, I. Dabo, A. Dal Corso, S. de Gironcoli, S. Fabris, G. Fratesi, R. Gebauer, U. Gerstmann, C. Gougousis, A. Kokalj, M. Lazzeri, L. Martin-Samos, N. Marzari, F. Mauri, R. Mazzarello, S. Paolini, A. Pasquarello, L. Paulatto, C. Sbraccia, S. Scandolo, G. Sclauzero, A. P. Seitsonen, A. Smogunov, P. Umari, R. M. Wentzcovitch, QUANTUM ESPRESSO: a modular and open-source software project for quantum simulations of materials, *J. Phys.: Condens. Matter* **21**, 395502(2009).
- [36] R. Y. Chen, S. J. Zhang, J. A. Schneeloch, C. Zhang, Q. Li, G. D. Gu, and N. L. Wang, Optical spectroscopy study of the three-dimensional Dirac semimetal ZrTe<sub>5</sub>, *Phys. Rev. B* **92**, 075107 (2015).
- [37] B. Xu, Y. M. Dai, L. X. Zhao, K. Wang, R. Yang, W. Zhang, J. Y. Liu, H. Xiao, G. F. Chen, A. J. Taylor, D. A. Yarotski, R. P. Prasankumar, and X. G. Qiu, Optical spectroscopy of the Weyl semimetal TaAs, *Phys. Rev. B* **93**, 121110(R) (2016).
- [38] D. Neubauer, J. P. Carbotte, A. A. Nateprov, A. Löhle, M. Dressel, and A. V. Pronin, Interband optical conductivity of the [001]-oriented Dirac semimetal Cd<sub>3</sub>As<sub>2</sub>, *Phys. Rev. B* **93**, 121202(R) (2016).
- [39] A. J. Frenzel, C. C. Homes, Q. D. Gibson, Y. M. Shao, K. W. Post, A. Charnukha, R. J. Cava, and D. N. Basov, Anisotropic electrodynamics of type-II Weyl semimetal candidate WTe<sub>2</sub>, *Phys. Rev. B* **95**, 245140 (2017).
- [40] S.-i. Kimura, H. Yokoyama, H. Watanabe, J. Sichelschmidt, V. Süß, M. Schmidt, and C. Felser, Optical signature of Weyl electronic structures in tantalum pnictides TaPn (Pn = P, As), *Phys. Rev. B* **96**, 075119 (2017).
- [41] F. Hütt, A. Yaresko, M. B. Schilling, C. Shekhar, C. Felser, M. Dressel, and A. V. Pronin, Linear-in-Frequency Optical Conductivity in GdPtBi due to Transitions near the Triple Points, *Phys. Rev. Lett.* **121**, 176601 (2018).
- [42] M. Dressel and G. Grüner, *Electrodynamics of Solids* (Cambridge University Press, Cambridge, 2002).
- [43] D. Wu, N. Barišić, P. Kallina, A. Faridian, B. Gorshunov, N. Drichko, L. J. Li, X. Lin, G. H. Cao, Z. A. Xu, N. L. Wang, and M. Dressel, Optical investigations of the normal and superconducting states reveal two electronic subsystems in iron pnictides, *Phys. Rev. B* **81**, 100512(R) (2010).
- [44] M. B. Schilling, A. Löhle, D. Neubauer, C. Shekhar, C. Felser, M. Dressel, and A. V. Pronin, Two-channel conduction in YbPtBi, *Phys. Rev. B* **95**, 155201 (2017).
- [45] D. Neubauer, A. Yaresko, W. Li, A. Löhle, R. Hübner, M. B. Schilling, C. Shekhar, C. Felser, M. Dressel, and A. V. Pronin, Optical conductivity of the Weyl semimetal NbP, *Phys. Rev. B* **98**, 195203 (2018).
- [46] R. Kemmler, R. Hübner, A. Löhle, D. Neubauer, I. Voloshenko, L. M. Schoop, M. Dressel and A. V. Pronin, Free-carrier dynamics in Au<sub>2</sub>Pb probed by optical conductivity measurements, *J. Phys.: Condens. Matter* **30**, 485403 (2018).
- [47] Z. Qiu, C. Le, Z. Liao, B. Xu, R. Yang, J. Hu, Y. Dai, and X. Qiu, Observation of a topological nodal-line semimetal in YbMnSb<sub>2</sub> through optical spectroscopy, *Phys. Rev. B* **100**, 125136 (2019).
- [48] R. Yang, M. Corasaniti, C. C. Le, Z. Y. Liao, A. F. Wang, Q. Du, C. Petrovic, X. G. Qiu, J. P. Hu, and L. Degiorgi, Spin-Canting-Induced Band Reconstruction in the Dirac Material Ca<sub>1-x</sub>Na<sub>x</sub>MnBi<sub>2</sub>, *Phys. Rev. Lett.* **124**, 137201

- (2020).
- [49] C. C. Homes, T. Wolf, and C. Meingast, Anisotropic optical properties of detwinned  $\text{BaFe}_2\text{As}_2$ , *Phys. Rev. B* **102**, 155135 (2020).
- [50] S. Polatkan and E. Uykur, Optical Response of Chiral Multifold Semimetal  $\text{PdGa}$ , *Crystals* **11**, 80 (2021).
- [51] D. Chaudhuri, B. Cheng, A. Yaresko, Q. D. Gibson, R. J. Cava, and N. P. Armitage, Optical investigation of the strong spin-orbit-coupled magnetic semimetal  $\text{YbMnBi}_2$ , *Phys. Rev. B* **96**, 075151 (2017).
- [52] M. Corasaniti, R. Yang, A. Pal, M. Chinotti, L. Degiorgi, A. Wang, and C. Petrovic, Fermi surface gapping in the Dirac material  $\text{Ca}_{1-x}\text{Na}_x\text{MnBi}_2$ , *Phys. Rev. B* **100**, 041107(R) (2019).
- [53] K. Schwarz and P. Blaha, Solid state calculations using WIEN2k, *Comput. Mater. Sci.* **28**, 259 (2003).